AFLOW-QHA3P: Robust and automated method to compute thermodynamic properties of solids

Pinku Nath,[1,2] Demet Usanmaz,[1,2] David Hicks,[1,2] Corey Oses,[1,2] Marco Fornari,[3,2] Marco Buongiorno Nardelli,[4,2] Cormac Toher,[1,2] and Stefano Curtarolo[1,2,5,*]

[1]*Department of Mechanical Engineering and Materials Science, Duke University, Durham, North Carolina 27708, USA*
[2]*Center for Materials Genomics, Duke University, Durham, North Carolina 27708, USA*
[3]*Department of Physics, Central Michigan University, Mount Pleasant, Michigan 48858, USA*
[4]*Department of Physics and Department of Chemistry, University of North Texas, Denton, Texas 76203, USA*
[5]*Fritz-Haber-Institut der Max-Planck-Gesellschaft, 14195 Berlin-Dahlem, Germany*

Accelerating the calculations of finite-temperature thermodynamic properties is a major challenge for rational materials design. Reliable methods can be quite expensive, limiting their applicability in autonomous high-throughput workflows. Here, the three-phonon quasiharmonic approximation (QHA) method is introduced, requiring only three phonon calculations to obtain a thorough characterization of the material. Leveraging a Taylor expansion of the phonon frequencies around the equilibrium volume, the method efficiently resolves the volumetric thermal expansion coefficient, specific heat at constant pressure, the enthalpy, and bulk modulus. Results from the standard QHA and experiments corroborate the procedure, and additional comparisons are made with the recently developed self-consistent QHA. The three approaches—three-phonon, standard, and self-consistent QHAs—are all included within the open-source *ab initio* framework AFLOW, allowing the automated determination of properties with various implementations within the same framework.

I. INTRODUCTION

Reliable and efficient computational methods are needed to guide time-consuming and laborious experimental searches, thus accelerating materials design. Implementing effective methods within automated frameworks such as AFLOW [1–5] facilitates the calculation of thermodynamic properties for large materials databases. There are several computational techniques to characterize the temperature-dependent properties of materials, each with varying accuracy and computational cost. Techniques such as *ab initio* molecular dynamics [6–10] and the stochastic self-consistent harmonic approximation [11,12] give accurate results for the temperature-dependent properties of materials. Although these methods are highly accurate, the treatment of anharmonicity requires the consideration of many large distorted structural configurations, making them computationally prohibitive for screening large materials sets. Other methods—including the Debye-Grüneisen model [13,14] and machine learning approaches [15,16]—require less computational resources, but often struggle to predict properties such as the Grüneisen parameter with reasonable accuracy [17,18]. The quasiharmonic approximation (QHA) [19–21] balances accuracy and computational cost for calculating temperature and pressure-dependent properties of materials.

In its standard formulation, QHA also remains too expensive for automated screening [22]. QHA requires many independent phonon spectra calculations, obtained by diagonalizing the dynamical matrices giving eigenvectors (modes)

and eigenvalues (energies) [23–26]. The dynamical matrix can be constructed either with a linear response [26,27] or the finite displacement method [26,28,29]. Despite its low computational demands, linear response does not perform well at high temperatures where anharmonicity can be large. The finite displacement method can be easily integrated with a routine that computes forces, making it the preferred method for high-throughput calculations. However, it is still computationally expensive for (i) low-symmetry crystals, (ii) materials with large atomic variations leading to complicated optical branches, and (iii) metallic systems having long-range force interactions requiring large supercells. To make QHA better suited for automated screening, it is necessary to reduce the number of required phonon spectra.

Recently, the self-consistent quasiharmonic approximation [30] (SC-QHA) has been developed. It self-consistently minimizes the external and internal pressures. The method requires spectra at only two or three volumes, while the frequency-volume relationship is determined using a Taylor expansion. It is computationally efficient and almost five times faster than QHA. Results agree well with experiments at low temperatures, although some deviations are observed at high temperatures for the tested systems [30].

In this article, the quasiharmonic approximation three-phonon (QHA3P) method is introduced. It calculates the phonon frequencies around equilibrium for only three different volumes, and performs a Taylor expansion to extrapolate the phonon frequencies at other volumes. The QHA3P approach drastically reduces the computational cost and achieves consistency with experiments, allowing automated materials' property screening without compromising accuracy. Similar to QHA, QHA3P minimizes the Helmholtz free

*stefano@duke.edu

energy with respect to volume for each temperature. The calculations of thermodynamic properties and the temperature-dependent electronic contribution to the free energy are the same as in QHA. The QHA, SC-QHA, and QHA3P methods are all implemented within AFLOW [1–5,22]. The performance of QHA3P with two different exchange-correlation (XC) functionals is investigated.

II. COMPUTATIONAL DETAILS

The thermal properties of materials at finite temperatures are calculated from the Helmholtz free energy (F), which depends on temperature (T) and volume (V). Neglecting the electron-phonon coupling and magnetic contributions, F can be written as the sum of three additive contributions [19–21],

$$F(V, T) = E_0(V) + F_{\text{vib}}(V, T) + F_{\text{elec}}(V, T), \quad (1)$$

where E_0 is the total energy of the system at 0 K without any atomic vibrations, F_{vib} is the vibrational free energy of the lattice ions, and F_{elec} is the finite-temperature electronic free energy due to thermal electronic excitations.

A. QHA methodology

QHA enables the calculation of F_{vib} via the harmonic approximation and includes anharmonic effects in the form of volume-dependent phonon frequencies. F_{vib} is given by [19–22]

$$
F_{\text{vib}}(V, T) \\
= \frac{1}{N_q} \sum_{\mathbf{q}, j} \left\{ \frac{\hbar \omega_j(\mathbf{q})}{2} + k_{\text{B}} T \ln \left[1 - \exp \left(-\frac{\hbar \omega_j(\mathbf{q})}{k_{\text{B}} T} \right) \right] \right\},
$$

$$(2)$$

where $\hbar$ and k_{B} are the Planck and Boltzmann constants, and $\omega_j(\mathbf{q})$ is the volume-dependent phonon frequency. The $(\mathbf{q}, j)$ comprises both the wave vector $\mathbf{q}$ and phonon branch index j. N_q is the total number of wave vectors.
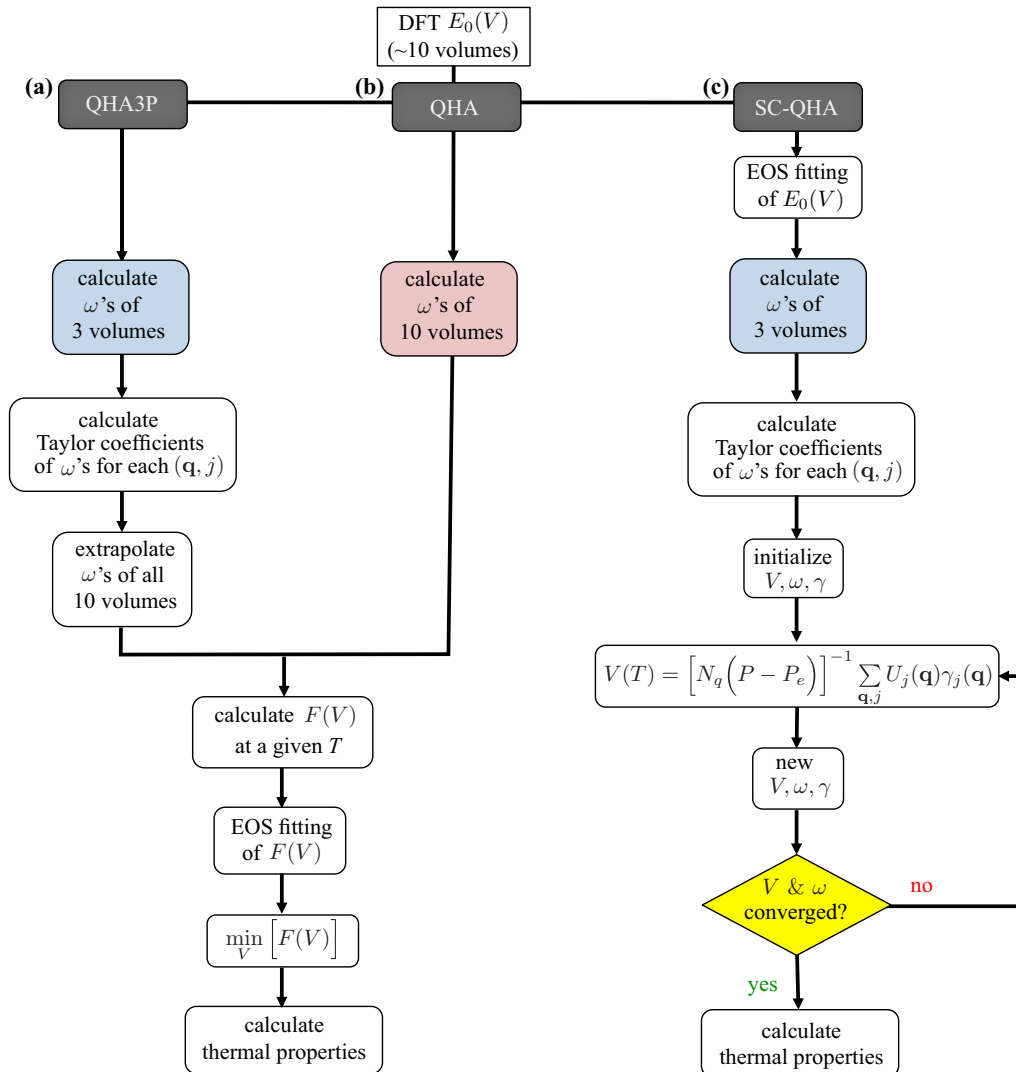

FIG. 1. The workflows for (a) QHA3P compared with (b) QHA and (c) SC-QHA. The most time-consuming step of QHA is highlighted in red, while the time-saving steps of the other two methods are highlighted in blue.

Although $F_{\text{elec}}(V, T)$ is negligible for wide band-gap materials, its contribution is required for metals and narrow band-gap systems. $F_{\text{elec}}(V, T)$ is calculated as [19,20,31]

$$F_{\text{elec}}(V, T) = U_{\text{elec}}(V, T) - T S_{\text{elec}}(V, T),$$

$$U_{\text{elec}}(V, T) = \int_0^\infty n_{\text{elec}}(\epsilon) f(\epsilon) \epsilon \, d\epsilon - \int_0^{E_F} n_{\text{elec}}(\epsilon) \epsilon \, d\epsilon,$$

$$S_{\text{elec}}(V, T) = -k_B \int_0^\infty n_{\text{elec}}(\epsilon) \{ f(\epsilon) \ln[f(\epsilon)]$$
$$+ [1 - f(\epsilon)] \ln[1 - f(\epsilon)] \} d\epsilon, \quad (3)$$

where $U_{\text{elec}}(V, T)$ and $S_{\text{elec}}(V, T)$ are the temperature-dependent parts of the electronic internal energy and electronic entropy, respectively, $n_{\text{elec}}(\epsilon)$ is the density of states at energy ϵ, $f(\epsilon)$ is the Fermi-Dirac distribution, and E_F is the Fermi energy.

The QHA method requires at least ~ 10 E_0 and ~ 10 phonon calculations (F_{vib}) to obtain a good fit for the equation of state (EOS). Generally, QHA employs isotropic volume distortions, although its implementation in AFLOW also incorporates anisotropic effects by considering F as a function of direction-dependent strain, e.g., along principal directions [32,33]. The calculated E_0 and F_{vib} are fitted to an EOS (e.g., Birch-Murnaghan EOS [34]). The equilibrium volume (V_{eq}) at a given temperature is determined by minimizing F with respect to V at a given T, $(\partial F/\partial V)_T = 0$ [Fig. 1(b)]. A more detailed description of F-V interpolation and the calculation of different energy terms is discussed in Ref. [22].

The thermodynamic properties—constant volume specific heat (C_V), constant pressure specific heat (C_P), average Grüneisen parameter ($\bar{\gamma}$), and volumetric thermal expansion coefficient (α_V) [19–22]—are calculated according to the following definitions:

$$C_V = \frac{k_B}{N_q} \sum_{\mathbf{q}, j} c_j(\mathbf{q}), \quad (4)$$

$$c_j(\mathbf{q}) = \left(\frac{\hbar \omega_j(\mathbf{q}, V_0)}{k_B T} \right)^2 \frac{\exp\left(\frac{\hbar \omega_j(\mathbf{q}, V_0)}{k_B T} \right)}{\left[\exp\left(\frac{\hbar \omega_j(\mathbf{q}, V_0)}{k_B T} \right) - 1 \right]^2}, \quad (5)$$

$$C_P = C_V + V_{\text{eq}} T B \alpha_V^2, \quad (6)$$

$$\bar{\gamma} = \frac{\sum_{\mathbf{q}, j} \gamma_j(\mathbf{q}) c_j(\mathbf{q})}{\sum_{\mathbf{q}, j} c_j(\mathbf{q})}, \quad (7)$$

$$\alpha_V = \frac{C_V \bar{\gamma}}{B V_{\text{eq}}}, \quad (8)$$

where $\omega_j(\mathbf{q}, V_0)$ is the frequency of phonon mode $(\mathbf{q}, j)$ at relaxed volume (V_0), and $c_j(\mathbf{q})$ and $\gamma_j(\mathbf{q})$ are the specific heat capacity at constant volume and mode Grüneisen parameter at $(\mathbf{q}, j)$. The definitions of the bulk modulus (B) and mode Grüneisen parameter [$\gamma_j(\mathbf{q})$] are

$$B = V_{\text{eq}} \left(\frac{\partial^2 F}{\partial V^2} \right)_T, \quad (9)$$

$$\gamma_j(\mathbf{q}) = -\frac{V_0}{\omega_j(\mathbf{q}, V_0)} \left(\frac{\partial \omega_j(\mathbf{q})}{\partial V} \right)_{V_0}. \quad (10)$$

For metals and small band-gap materials, the electronic contribution can be considerable and is included in the thermodynamic definitions. α_V and C_P are reformulated as [33,35]

$$\alpha_{V, \text{ph+elec}} = \alpha_V + \alpha_{V, \text{elec}} = \frac{C_V \bar{\gamma}}{B V_{\text{eq}}} + \frac{2}{3 B V_{\text{eq}}} C_{V, \text{elec}},$$

$$C_{P, \text{ph+elec}} = C_V + V_{\text{eq}} T B \alpha_V^2 + C_{V, \text{elec}},$$

$$C_{V, \text{elec}} = T \left(\frac{\partial S_{\text{elec}}}{\partial T} \right)_V. \quad (11)$$

In addition to the basic quasiharmonic thermodynamic properties, the enthalpy (H) of a structure at $P = 0$ [21,31] is

$$H = F(T) + TS = F(T) - T \frac{\partial F(T)}{\partial T}. \quad (12)$$

B. AFLOW implementation of SC-QHA

SC-QHA has been implemented within AFLOW following the description of Ref. [30]. Similar to QHA, SC-QHA calculates E_0 at ~ 10 different volumes, but requires only three phonon calculations at different cell volumes [Fig. 1(c)] [30]. It computes the temperature-dependent unit-cell volume by optimizing the total pressure (external, electronic, and

TABLE I. Compound names with ICSD number, supercell size, supercell atoms, lattice type, and space group number. More detailed information is available in Table II.

Compound	ICSD	Supercell size	Supercell atoms	Lattice type	SG No.
Si	76268	$5 \times 5 \times 5$	250	fcc	227
C (Diamond)	28857	$4 \times 4 \times 4$	128	fcc	227
SiC	618777	$4 \times 4 \times 3$	192	hex	186
Al$_2$O$_3$	89664	$2 \times 2 \times 2$	80	rhl	167
MgO	159372	$4 \times 4 \times 4$	128	fcc	225
ZnO	182356	$4 \times 4 \times 3$	192	hex	186
AlNi	602150	$4 \times 4 \times 4$	128	cub	221
NiTiSn	174568	$3 \times 3 \times 3$	81	fcc	216
Ti$_2$AlN	157766	$4 \times 4 \times 1$	128	hex	194

vibrational pressures),

$$V = [(P - P_e)]^{-1} \times \frac{1}{N_q} \sum_{\mathbf{q}, j} U_j(\mathbf{q}) \gamma_j(\mathbf{q}), \qquad (13)$$

where P is the external pressure, P_e ($= -dE_0(V)/dV$) is the electronic pressure, $U_j(\mathbf{q})$ is the mode vibrational internal energy, and $\gamma_j(\mathbf{q})$ is the mode Grüneisen parameter at $(\mathbf{q}, j)$. The volume-dependent $\omega_j(\mathbf{q})$ and $\gamma_j(\mathbf{q})$ are extrapolated to other
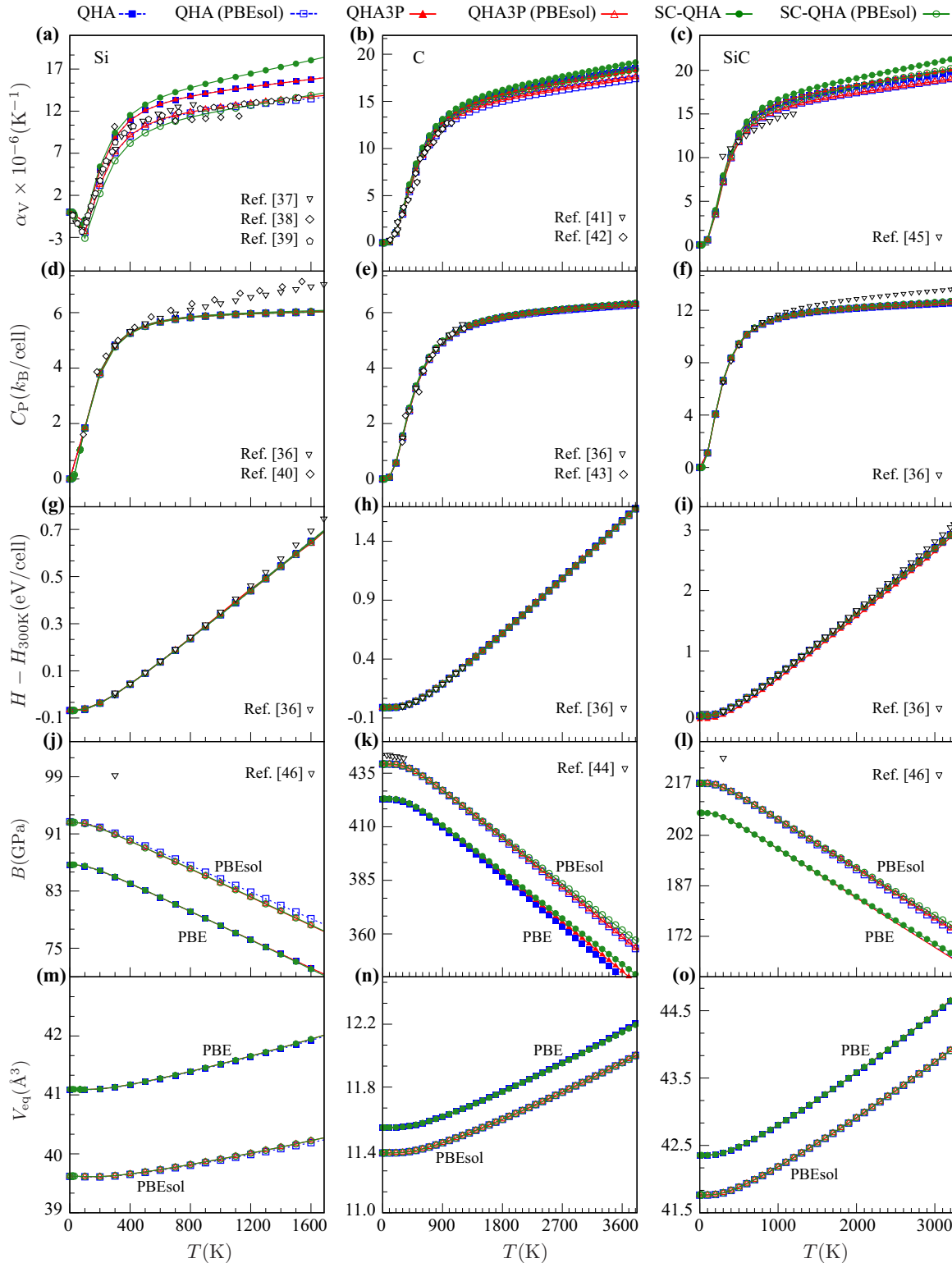

FIG. 2. The thermodynamic properties of Si [(a), (d), (g), (j), (m)], C [(b), (e), (h), (k), (n)], and SiC [(c), (f), (i), (l), (o)] are presented up to their melting temperatures: 1687, 3823, and 3000 K [36], respectively. The results are obtained with QHA, QHA3P, and SC-QHA using the PBE and PBEsol XC functionals. Experimental results from different sources [36–46] are indicated by inverted triangles, diamonds, and pentagons.
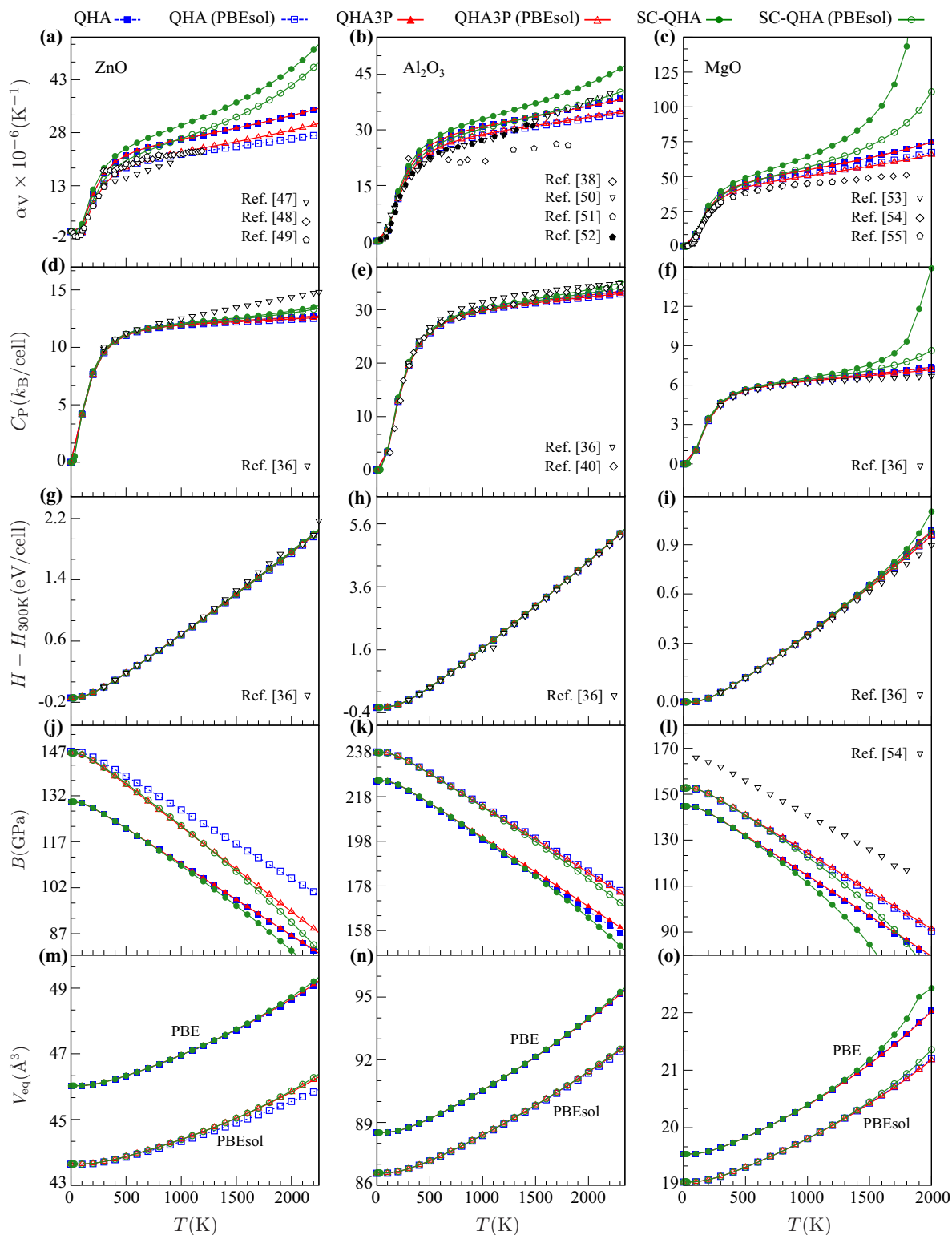
FIG. 3. The thermodynamic properties of ZnO [(a), (d), (g), (j), (m)], Al_2O_3 [(b), (e), (h), (k), (n)], and MgO [(c), (f), (i), (l), (o)] as a function of temperature. The results of ZnO and Al_2O_3 are presented up to their melting temperatures (T_m), while MgO is shown up to $(2/3)T_m$. The T_m values of ZnO, Al_2O_3, and MgO are 2248, 2345, and 3125 K [36], respectively. The results are obtained with QHA, QHA3P, and SC-QHA using the PBE and PBEsol XC functionals. Experimental results from different sources [36,38,40,47–55] are indicated by inverted triangles, diamonds, pentagons, and solid pentagons.

TABLE II. List of compound names with various crystallographic properties along with the AFLOW prototype [69,70] and unique identifier (auid) [5].

Compound	ICSD	Supercell size	Supercell atoms	Lattice type	SG No.	DFT band gap (eV)	Prototype	auid
Si	76268	$5 \times 5 \times 5$	250	fcc	227	0.61	A_cF8_227_a [71]	aflow:ff211836be789f69
C (Diamond)	28857	$4 \times 4 \times 4$	128	fcc	227	4.11	A_cF8_227_a [71]	aflow:b438e1a25f9c187d
SiC	618777	$4 \times 4 \times 3$	192	hex	186	2.30	AB_hP4_186_b_b [72]	aflow:504844a24702c7dc
ZnO	182356	$4 \times 4 \times 3$	192	hex	186	1.81	AB_hP4_186_b_b [72]	aflow:f30df164c6192045
Al_2O_3	89664	$2 \times 2 \times 2$	80	rhl	167	5.86	A2B3_hR10_167_c_e [73]	aflow:537e800e0a1b75be
MgO	159372	$4 \times 4 \times 4$	128	fcc	225	4.46	AB_cF8_225_a_b [74]	aflow:a2cc05c200330e16
AlNi	602150	$4 \times 4 \times 4$	128	cub	221	0.00	AB_cP2_221_b_a [75]	aflow:f727dcd6a292301d
NiTiSn	174568	$3 \times 3 \times 3$	81	fcc	216	0.17	ABC_cF12_216_b_c_a [76]	aflow:7bed936e9d5a44ca
Ti_2AlN	157766	$4 \times 4 \times 1$	128	hex	194	0.00	ABC2_hP8_194_d_a_f [77]	aflow:bdc38ae3ca07e398

volumes using a Taylor expansion,

$$\omega_j(\mathbf{q}, V) = \omega_j(\mathbf{q}, V_0) + \left(\frac{\partial \omega_j(\mathbf{q})}{\partial V}\right)_{V_0} (\Delta V)$$
$$+ \frac{1}{2}\left(\frac{\partial^2 \omega_j(\mathbf{q})}{\partial V^2}\right)_{V_0} (\Delta V)^2, \quad (14)$$

$$\gamma_j(\mathbf{q}, V) = -\frac{V}{\omega_j(\mathbf{q})}\left[\left(\frac{\partial \omega_j(\mathbf{q})}{\partial V}\right)_{V_0} + \left(\frac{\partial^2 \omega_j(\mathbf{q})}{\partial V^2}\right)_{V_0} \Delta V\right], \quad (15)$$

where $\Delta V = V - V_0$. Computing the second-order derivative of $\omega_j(\mathbf{q})$ requires the calculation of phonon spectra at three different volumes. Due to its numerical accuracy, the central difference algorithm is used to calculate the derivative with respect to volume. $U_j(\mathbf{q})$, the mode vibrational internal energy, is defined as

$$U_j(\mathbf{q}) = \left\{\left[\exp\left(\frac{\hbar \omega_j(\mathbf{q})}{k_B T}\right) - 1\right]^{-1} + \frac{1}{2}\right\}\hbar \omega_j(\mathbf{q}). \quad (16)$$

The procedure to self-consistently optimize the volume at zero external pressure ($P = 0$) and finite T is as follows [30] [Fig. 1(c)]:

(1) First, ~ 10 $E_0(V)$ values are fitted to the EOS, enabling the analytical calculation of P_e at any new volume.

(2) $[\partial \omega_j(\mathbf{q})/\partial V]_{V_0}$ and $[\partial^2 \omega_j(\mathbf{q})/\partial V^2]_{V_0}$ are calculated from the three phonon spectra, where $\omega_j(\mathbf{q})$ and $\gamma_j(\mathbf{q})$ are initialized to their values at V_0.

(3) To compute the equilibrium volume at T, V is initialized to a value 0.2% larger than V_0 and the following loop is iterated:

(i) Calculate P_e using the EOS, and $\sum_{\mathbf{q},j} U_j(\mathbf{q})\gamma_j(\mathbf{q})$ using $\omega_j(\mathbf{q})$ and $\gamma_j(\mathbf{q})$.

(ii) Update the value of V using Eq. (13), and update $\omega_j(\mathbf{q})$ and $\gamma_j(\mathbf{q})$ using Eqs. (14) and (15), respectively.

(iii) If V is not converged to within an acceptable threshold (e.g., 10^{-6}), then loop over steps (i) and (ii).

(iv) Calculate other thermodynamic properties using the converged values of $\omega_j(\mathbf{q})$ and $\gamma_j(\mathbf{q})$.

(v) V, $\omega_j(\mathbf{q})$, and $\gamma_j(\mathbf{q})$ at a given T become the initial values for the next T characterization.
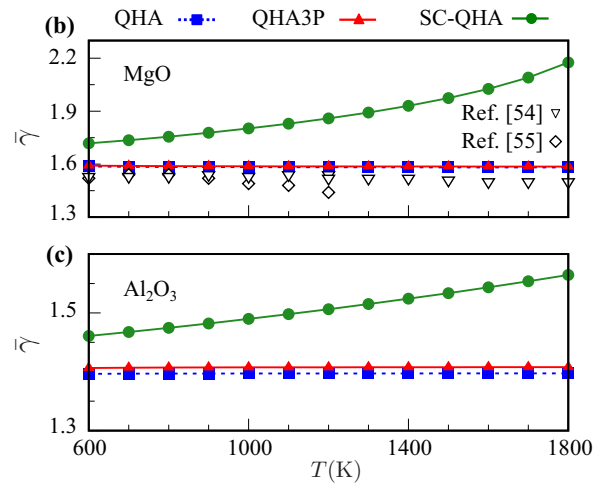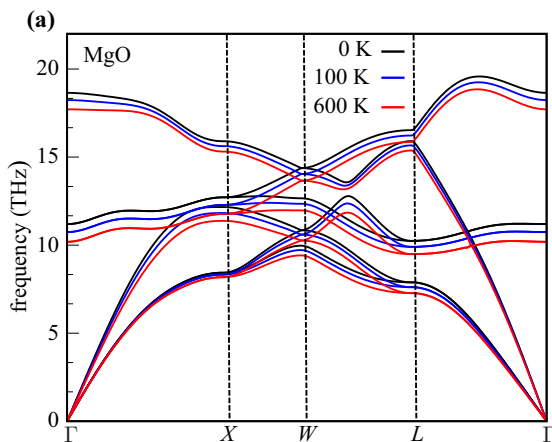

FIG. 4. (a) The phonon dispersion curves of MgO at three different temperatures are computed using SC-QHA equilibrium volumes and Eq. (14). (b), (c) The $\bar{\gamma}$ values as a function of temperature for MgO and Al_2O_3 using QHA, QHA3P, and SC-QHA. The experimental Grüneisen parameters of MgO are taken from Refs. [54,55].

In SC-QHA, V_{eq} is calculated self-consistently at low temperatures (e.g., 0.1 K). At higher temperatures, V_{eq} is extrapolated as $V_{eq}(T + \Delta T) \simeq (1 + \alpha_V \Delta T)V_{eq}$—as described in Ref. [30]—to avoid self-consistent volume calculations for each T. V_{eq} is equal to the self-consistently converged V at a given T. Similarly, all properties calculated at V_{eq} are the equilibrium properties at T.

While C_V, C_P, and α_V are the same as for QHA, B and $\gamma_j(\mathbf{q})$ are computed differently in SC-QHA,

$$B = V_{eq}\left(\frac{d^2 E_0}{dV^2}\right)_{V_{eq}} + B_\gamma + B_{\Delta\gamma} + P_\gamma, \qquad (17)$$

where B_γ and $B_{\Delta\gamma}$ are the bulk modulus contributions due to phonons, and P_γ represents the bulk modulus contribution due to external pressure. The mathematical expressions for these variables are defined in Ref. [30], and $\gamma_j(\mathbf{q})$ is computed using Eq. (15). It is also important to note that the value of C_V at a given T is computed with the $\omega_j(\mathbf{q})$ values instead of $\omega_j(\mathbf{q}, V_0)$, where $\omega_j(\mathbf{q})$ is the volume- (and thus temperature-) dependent frequency.

The temperature-dependent electronic energy contributions can be added to SC-QHA by employing the relationship between the electronic eigenvalues and V [similar to the relationship between phonon eigenvalues and volume in Eq. (13)]. F_{elec} is not included in the version of SC-QHA implemented in AFLOW. Derivations and a more detailed description of SC-QHA can be found in Ref. [30]. The version of SC-QHA implemented in AFLOW is equivalent to the 2nd-SC-QHA [30].

C. QHA3P and QHA5P methodology

The QHA3P method requires only three phonon calculations along with the ~ 10 E_0 energies. The Taylor expansion [Eq. (14)] introduced in SC-QHA [30] is used to extrapolate the phonon spectra to the remaining volumes. The following
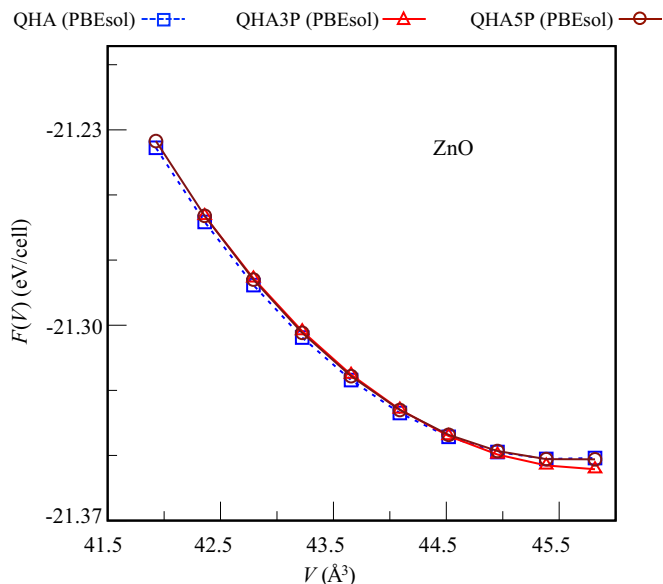
steps are the same as QHA: Fit to the EOS, minimize F with respect to V, and calculate the thermodynamic properties [Fig. 1(a)]. Although the same technique is used to extrapolate the phonon frequencies [Eq. (14)] in both QHA3P and SC-QHA, the definitions of some thermodynamic properties and the method for computing them differ. For example, the mode Grüneisen parameter is extrapolated with Eq. (15) in SC-QHA, but it is explicitly calculated using Eq. (10) in QHA3P. Therefore, inaccuracies in the phonon dispersion [$\omega_j(\mathbf{q})$] generally introduce more error in $\bar{\gamma}$ for SC-QHA compared to QHA3P.

The success of QHA3P depends on the estimation of $\omega_j(\mathbf{q})$ with the Taylor expansion coefficients. For some systems, the second-order Taylor expansion (QHA3P) is not sufficient to predict thermodynamic properties with good accuracy. Extending it to fourth order, which requires five phonon calculations (QHA5P), can improve reliability. The method has been developed and comparisons with QHA3P are included in Sec. III.

D. The root-mean-square relative deviation

The root-mean-square relative deviation (RMSrD)

$$\chi(X, Y) = \sqrt{\frac{\sum_i^N \left(\frac{X_i - Y_i}{X_i}\right)^2}{N - 1}} \qquad (18)$$

is used to quantitatively compare the calculated thermodynamic properties between the various methods and validate the model against experiments. Here, $\chi(X, Y)$ represents the RMSrD between N data points obtained from methods X and Y. Small values of $\chi(X, Y)$ indicate that X and Y produce statistically similar results.

E. Geometry optimization

All structures are fully relaxed using the high-throughput framework AFLOW, and density functional theory package VASP [56]. Optimizations are performed following the AFLOW Standard [57]. The projector augmented-wave (PAW) pseudopotentials [58] and the XC functionals proposed by Perdew-Burke-Ernzerhof (PBE) [59] are used for all calculations, unless otherwise stated. To study functional effects and compare with previous SC-QHA results [30], calculations using the PBEsol functional [60] are also carried out. A high-energy cutoff (40% larger than the maximum recommended cutoff among all the species) and a **k**-point mesh of 8000 **k**-points per reciprocal atom are used to ensure the accuracy of the results. Primitive cells are fully relaxed until the energy difference between two consecutive ionic steps is smaller than 10^{-9} eV and forces on each atom are below 10^{-8} eV/Å.

FIG. 5. The $F(V)$ curve of ZnO at 2000 K. The range of volumes is from -3% to 6% of V_0 (43.22 Å^3). The difference between any two curves gives F_{vib}, since E_0 is the same for QHA, QHA3P, and QHA5P.

F. Phonon calculations

Phonon calculations are carried out using the Automatic Phonon Library [29,61], as implemented in AFLOW, using VASP to obtain the interatomic force constants via the finite-displacements approach. The magnitude of this displacement is chosen as 0.015 Å. Supercell size and the number of atoms in the supercell (supercell atoms) along with space
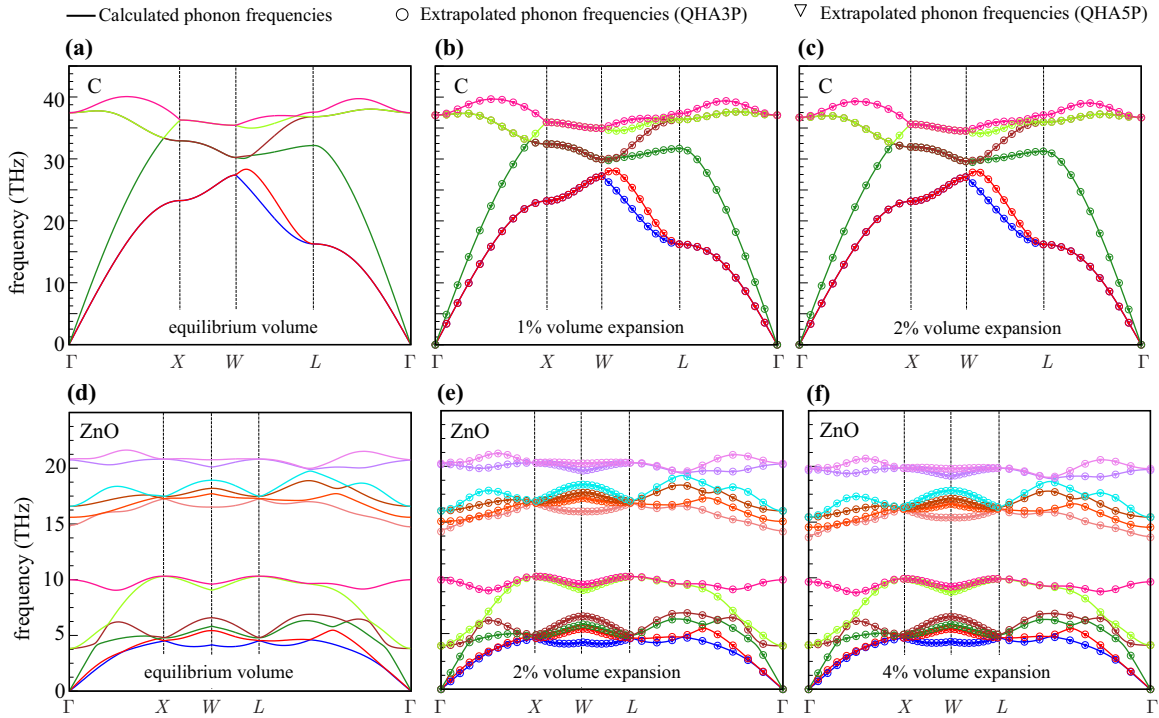
FIG. 6. Calculated and extrapolated (from the Taylor expansion) phonon dispersion curves for C [(a)–(c)] and ZnO [(d)–(f)] at their respective equilibrium volumes and two expanded volumes with the PBEsol XC functional. Phonon band continuity is highlighted using different colors. Note that the frequencies obtained using the Taylor expansion follow the same band continuity as the phonon dispersion obtained from QHA.

group number (SG No.) of each example [62] are listed in Table I. Nonanalytical contributions to the dynamical matrix are also included using the formulation developed by Wang *et al.* [63]. Frequencies and other related phonon properties are calculated on a $31 \times 31 \times 31$ mesh in the Brillouin zone: sufficient to converge the vibrational density of states and thus the corresponding thermodynamic properties. The phonon density of states is calculated using the linear interpolation tetrahedron technique available in AFLOW. The QHA calculations are performed on ten equally spaced volumes ranging from -3% to 6% uniform strain with 1% increments from the respective equilibrium structures of the crystal. The QHA Grüneisen parameter is calculated with $\pm 0.03\%$ distorted volumes [22]. More expanded (as opposed to compressed) volumes are used since most ma-

terials have positive thermal expansion. Both the SC-QHA and the QHA3P calculations employ $\pm 3\%$ expanded and compressed volumes. All calculations are performed without external pressure ($P = 0$), and all volume distortions are isotropic.

III. RESULTS AND DISCUSSION

A. Nonmetallic compounds

Thermodynamic properties for Si, C, and SiC are illustrated in Fig. 2 and ZnO, Al$_2$O$_3$, and MgO in Fig. 3. Comparisons of QHA3P with QHA, SC-QHA, and experimental data are discussed below with two different XC functionals.

TABLE III. RMSrD for α_V for all nonmetallic materials. χ for α_V are calculated with respect to the experiments in Ref. [39] (Si), Ref. [41] (C), Ref. [45] (SiC), Ref. [48] (ZnO), Ref. [50] (Al$_2$O$_3$), and Ref. [54] (MgO). Units: RMSrD in percent.

Compound	χ(QHA3P, QHA) % (α_V)		χ(SC-QHA, QHA) % (α_V)		χ(QHA3P, expt) % (α_V)		χ(SC-QHA, expt) % (α_V)	
	PBE	PBEsol	PBE	PBEsol	PBE	PBEsol	PBE	PBEsol
Si	0.1	1.3	9.2	7.5	15.7	8.4	25.8	19.6
C	0.8	1.0	2.8	4.5	14.0	12.1	16.8	12.4
SiC	0.7	0.4	4.7	3.7	13.5	12.7	12.6	11.1
ZnO	0.4	5.9	27.0	37.7	16.7	7.3	31.7	16.2
Al$_2$O$_3$	0.3	0.8	11.1	9.5	12.4	8.1	18.7	9.1
MgO	0.1	1.8	27.5	14.5	25.4	14.4	75.0	38.0

α_V from both QHA3P and QHA agree well with the available experiments for all tested nonmetallic compounds using both XC functionals. Conversely, SC-QHA overestimates α_V for Si, ZnO, Al$_2$O$_3$, and MgO. Using the PBEsol XC functional improves consistency with experimental results for Si, although α_V is still larger for ZnO and MgO. For Al$_2$O$_3$, α_V values from different experiments [38,50–52] vastly differ from one other. Below 1500 K, experimental
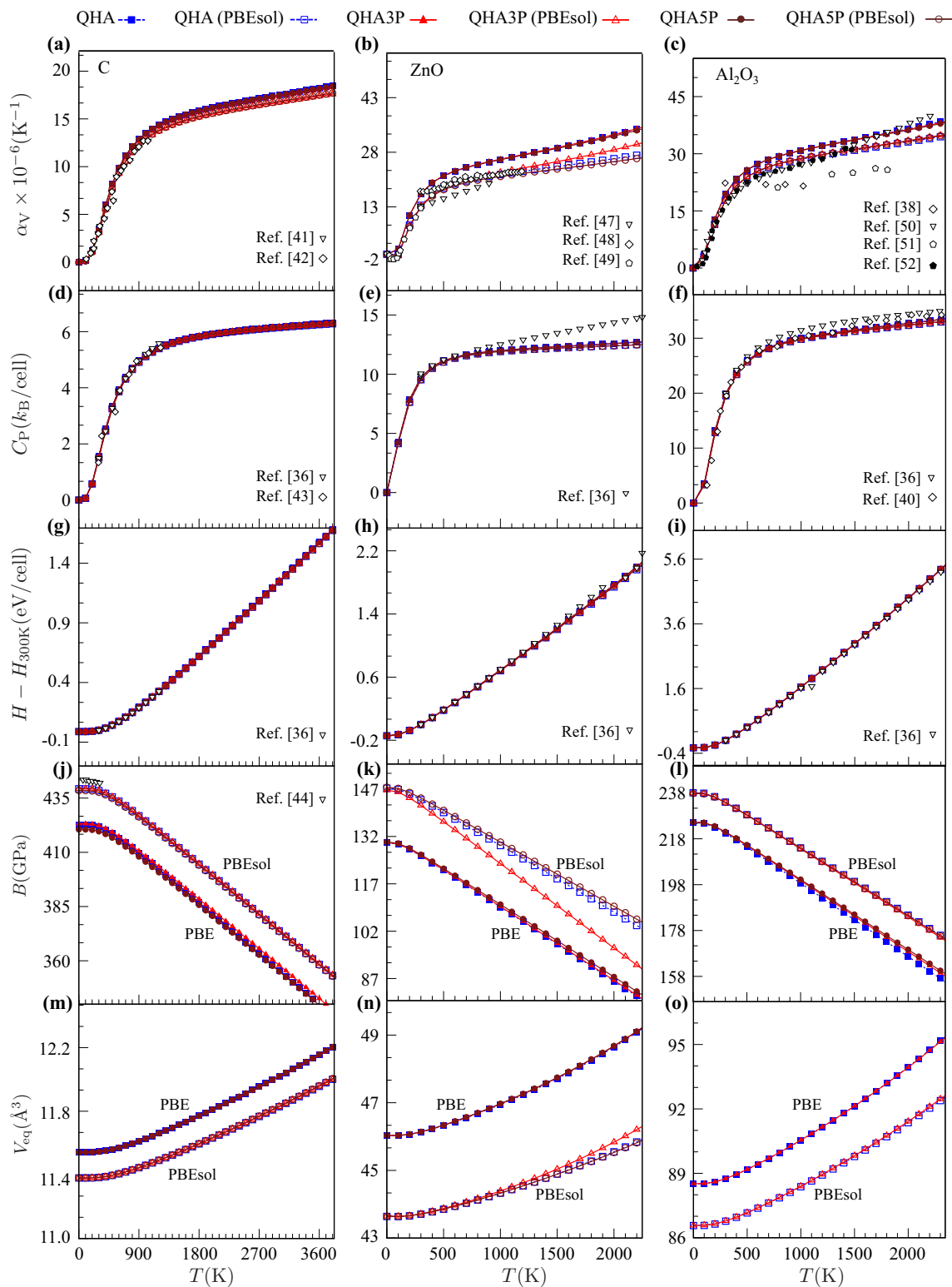

FIG. 7. The thermodynamic properties of C [(a), (d), (g), (j), (m)], ZnO [(b), (e), (h), (k), (n)], and Al$_2$O$_3$ [(c), (f), (i), (l), (o)] are presented up to their melting temperatures: 3823, 2248, and 2345 K [36], respectively. The results are obtained with QHA, QHA3P, and QHA5P using the PBE and PBEsol XC functionals. Experimental results from different sources [36,38,40–44,47–52] are indicated by inverted triangles, diamonds, pentagons, and solid pentagons.

TABLE IV. RMSrD for C_P and B for all nonmetallic materials. χ for C_P are calculated with respect to the experiments in Ref. [36]. χ for H and V_{eq} are similar to C_P and B, respectively, and are not presented. Units: RMSrD in percent.

Compound	χ(QHA3P, expt) % (C_P)		χ(SC-QHA, expt) % (C_P)		χ(QHA3P, QHA) % (B)		χ(SC-QHA, QHA) % (B)	
	PBE	PBEsol	PBE	PBEsol	PBE	PBEsol	PBE	PBEsol
Si	7.4	7.6	7.1	7.7	0.5	0.2	0.2	0.4
C	2.2	2.2	3.1	1.8	0.5	0.0	1.0	0.5
SiC	4.8	5.0	4.4	4.6	0.0	0.1	0.2	0.3
ZnO	8.5	9.3	5.9	7.0	0.3	7.0	3.4	9.8
Al$_2$O$_3$	4.5	5.3	3.0	4.1	0.8	0.3	1.1	1.7
MgO	9.0	3.6	37.1	11.5	0.5	0.7	21.6	6.6

results from Refs. [50,52] are well described by PBEsol, whereas above 1500 K, they are better predicted by PBE. The RMSrD between α_V from different approaches and experiments are provided in Table III. The relatively small RMSrD between QHA3P and experiments compared to the RMSrD between SC-QHA and experiments indicate that the QHA3P α_V predictions are more reliable.

The larger values of α_V from SC-QHA are due to the overestimation of $\bar{\gamma}$. This is particularly significant for positive α_V materials, where $\omega_j(\mathbf{q})$ decreases with T for almost all $(\mathbf{q}, j)$. For example, the T-dependent phonon dispersion curves of MgO [Fig. 4(a)] show that $\omega_j(\mathbf{q})$ decreases for all $(\mathbf{q}, j)$ except for acoustic branches near Γ. Figures 4(b) and 4(c) illustrate that the values of $\bar{\gamma}$ for MgO and Al$_2$O$_3$ are unaffected by the differences in volume distortion magnitudes between QHA and QHA3P and match well with experiments.

Despite deviations in α_V, there are no significant differences between C_P and H obtained from the three approaches. The values are insensitive to the choice of functional, except for MgO [Figs. 2(d)–2(i) and 3(d)–3(i)]. Both C_P and H match experimental values well. However, C_P is slightly underestimated for Si, SiC, and ZnO. Additionally, divergence from experiments occurs near 2000 K for MgO using the PBE XC functional in SC-QHA. The observations are supported by the RMSrD of C_P (Table IV).

The values of B computed with the three methodologies also match when using the same XC functional, except for ZnO and MgO [Figs. 2(j)–2(l) and 3(j)–3(l)]. For ZnO, discrepancies occur between the QHA3P and QHA results. Since the bulk modulus value is related to the curvature of $F(V)$ at V_{eq}, small changes in $F(V)$ can have a large impact on B. For instance, at 2000 K the difference in F between QHA3P and QHA for ZnO is approximately 5 meV at 6% expanded volume of V_0 (Fig. 5), significantly affecting B [Fig. 3(j)].

The values of B calculated using PBEsol are larger than for PBE, with similar trends reported previously [46], and are closer to experiment. For MgO, deviations occur at high temperatures between SC-QHA and QHA3P (and QHA). RMSrD with experiment for B has not been calculated due to limited data availability. For B, the small RMSrD values between QHA3P and QHA demonstrate that the methods are consistent with each other. Conversely, the RMSrD values between SC-QHA and QHA are high for ZnO and MgO (Table IV).

As for B, predicted V_{eq} values are similar for all methods when using the same XC functional. However, the volume predictions obtained using PBEsol are smaller than those for PBE [Figs. 2(m)–2(o) and 3(m)–3(o)].

Although features of the phonon spectra—including band continuity—are well predicted by the Taylor expansion (Fig. 6), $F(V)$ curves from QHA and QHA3P deviate in some cases (Fig. 5). In particular, discrepancies between QHA and QHA3P occur for ZnO with the PBEsol XC functional. Including higher-order terms in the Taylor expansion (QHA5P) eliminates the differences (Fig. 5) and improves the α_V, B, and V_{eq} values (Fig. 7).

B. Metallic compounds and narrow band-gap materials

Thermodynamic properties for metals AlNi and Ti$_2$AlN and narrow band-gap (0.12 eV [67]) half-Heusler NiTiSn are presented in Fig. 8. For QHA3P and QHA, calculations are performed with and without the electronic contribution. Results for SC-QHA are presented without the electronic contribution (not implemented in AFLOW). In this section, calculations are performed only with the PBE XC functional.

Similar to the nonmetallic examples, there are no prominent differences between α_V obtained using the three methods [Figs. 8(a)–8(c)]. The α_V results demonstrate the effectiveness

TABLE V. RMSrD for α_V, C_P, and H for metallic materials (AlNi and Ti$_2$AlN) and a small band-gap compound (NiTiSn). χ for α_V are computed with respect to the experiment in Ref. [20] (AlNi), Ref. [33] (NiTiSn), and Ref. [64] (Ti$_2$AlN). Units: RMSrD in percent. N/A: Not available.

Compound	χ(QHA3P, expt) % $(\alpha_{V,ph+elec})$	χ(QHA3P, expt) % (α_V)	χ(QHA3P, expt) % $(C_{P,ph+elec})$	χ(QHA3P, expt) % (C_P)	χ(QHA3P, expt) % $(H_{ph+elec})$	χ(QHA3P, expt) % (H)
AlNi	5.2	5.1	2.6	3.2	5.6	1.9
NiTiSn	6.4	6.2	0.0	0.0	N/A	N/A
Ti$_2$AlN	4.9	5.7	0.0	0.0	N/A	N/A

of all methodologies in accurately predicting the experimental thermodynamic properties of AlNi, NiTiSn, and Ti$_2$AlN. In addition, the contribution of F_{elec} to F does not alter the results.

The other thermodynamic properties—C_P, H, B, and V_{eq}— also match well with each other (for the three methods) and with experiments, with a few exceptions [Figs. 8(d)– 8(f)]. The H values for AlNi from QHA3P and QHA do
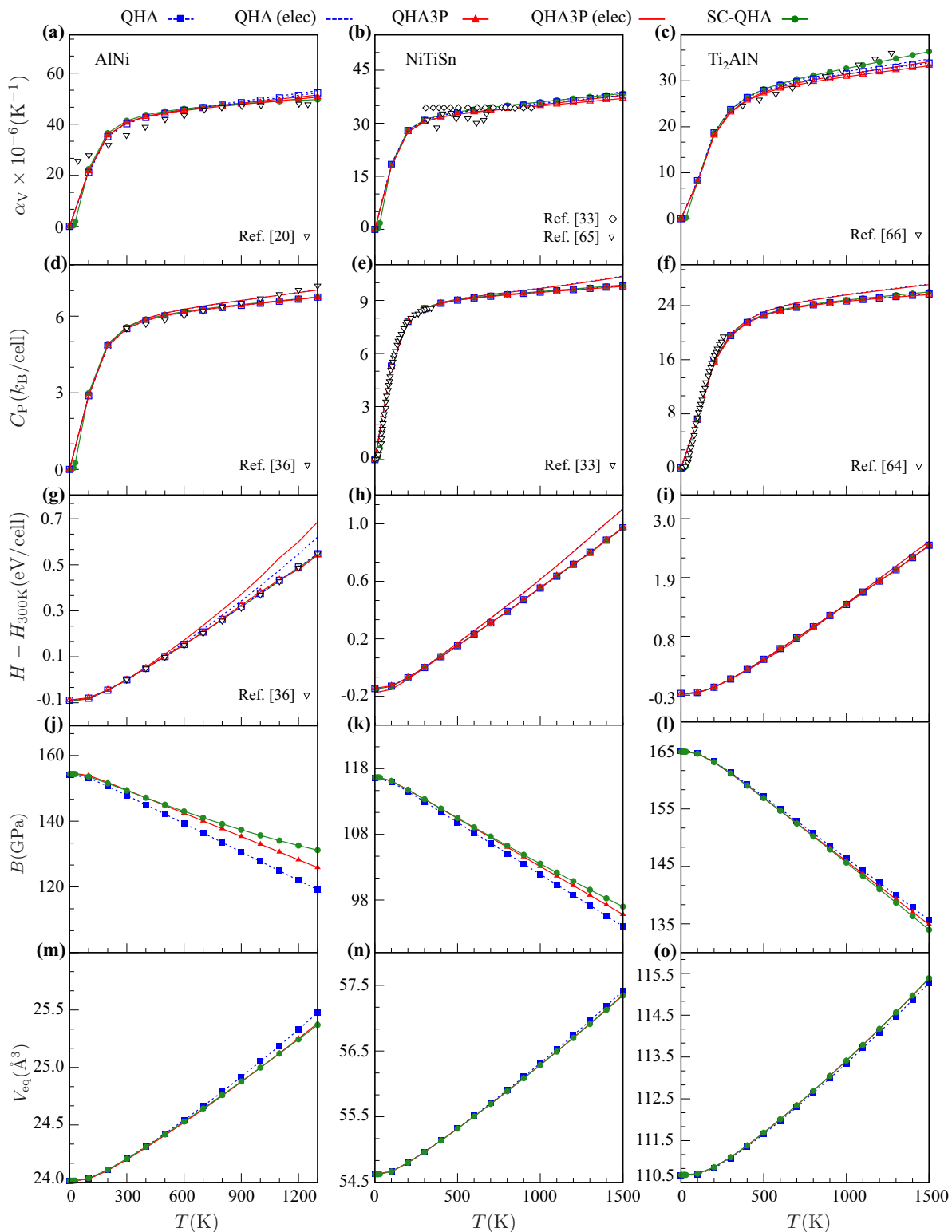

FIG. 8. The thermodynamic properties of AlNi [(a), (d), (g), (j), (m)], NiTiSn [(b), (e), (h), (k), (n)], and Ti$_2$AlN [(c), (f), (i), (l), (o)] are presented up to their melting temperatures of 1300, 1500, and 1500 K [20,33,64–66], respectively. QHA3P results are compared with QHA and experiments. Experimental results from different sources [20,33,36,64–66] are indicated by inverted triangles and diamonds.
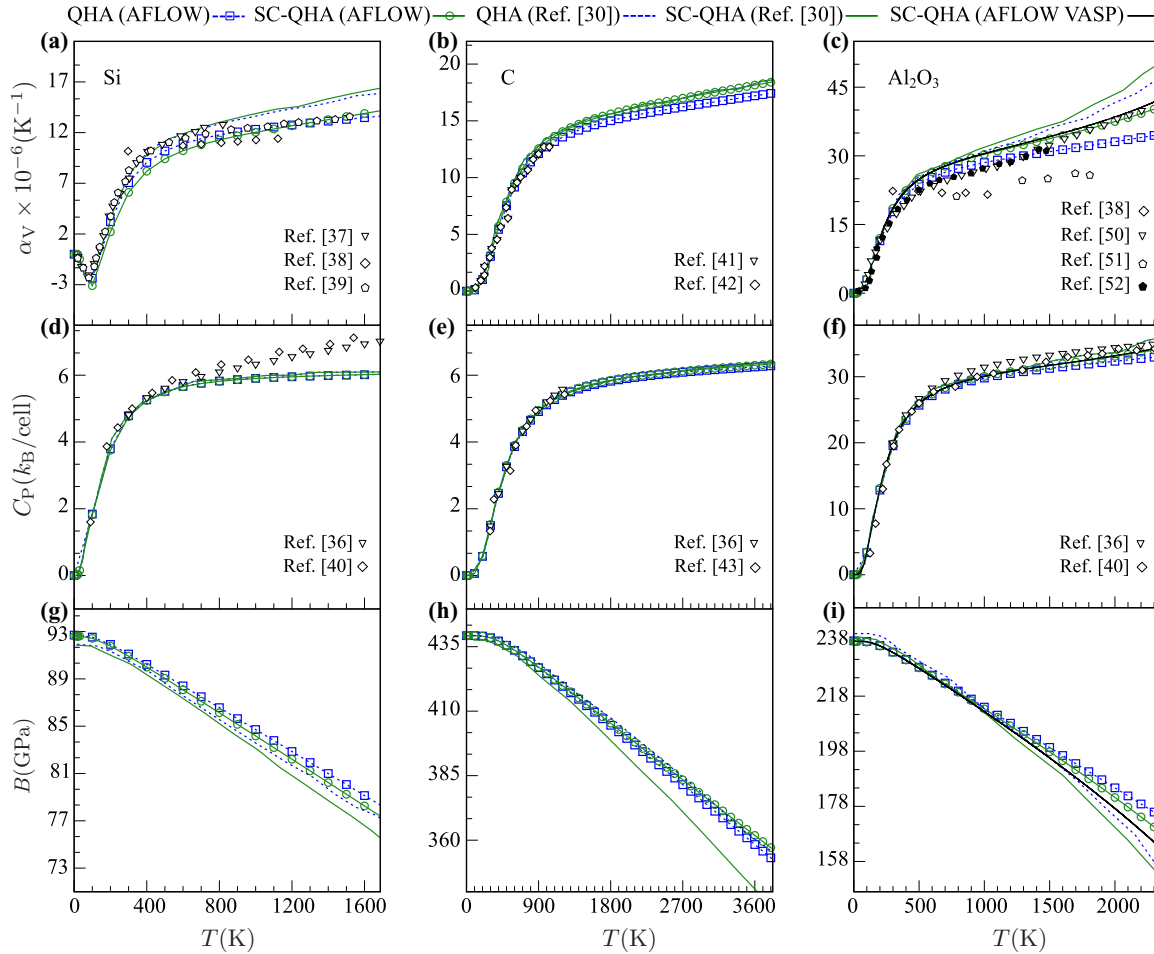
FIG. 9. Comparison of AFLOW computed α_V, C_P and B with Ref. [30]. Experimental results from different sources [36–43,50–52] are indicated by inverted triangles, diamonds, pentagons, and solid pentagons. The black line in the Al_2O_3 plots represents calculations with the PHONOPY+SC-QHA codes [30,68], performed using the AFLOW Standard VASP input parameters.

not agree with experiments above 500 K when F_{elec} is taken into consideration [Fig. 8(g)]. The B values from the three methods show discrepancies stemming from differences in the $F(V)$ energies. The small RMSrDs between QHA3P and experiments for α_V, C_P, and H demonstrate the reliability of the approach. Since the QHA, SC-QHA, and QHA3P predictions are similar, RMSrD values are presented only for QHA3P (Table V).

C. Comparison of SC-QHA implementation in AFLOW versus Ref. [30]

The SC-QHA method was originally developed and tested in Ref. [30] using the PBEsol XC functional. To check the consistency between the AFLOW implementation of SC-QHA and Ref. [30], the calculated properties are compared for Si, C, and Al_2O_3 (Fig. 9). The differences between the properties computed with AFLOW and Ref. [30] are marginal. However, some discrepancies are observed for the α_V values of Si, B values of C, and the α_V and B values of Al_2O_3, which are the presented examples in Ref. [30]. To investigate this, thermodynamic properties are reproduced for Al_2O_3 using the original SC-QHA and PHONOPY [68] codes with the AFLOW

Standard VASP input parameters (Fig. 9). This indicates that the origin of the incompatibility between these two studies is the difference in the VASP input parameters. While the accuracy is increased by using the AFLOW Standard VASP input parameters, the SC-QHA results are still inconsistent with QHA and experiments.

IV. CONCLUSIONS

The quasiharmonic approximation three-phonon method is introduced to calculate the thermodynamic properties of both nonmetallic and metallic compounds. The efficiency of QHA3P is tested for a range of materials using two different exchange-correlation functionals, and the calculated thermodynamic quantities are in agreement with both QHA and experimental measurements. We show that SC-QHA overestimates the average Grüneisen parameter, as well as α_V, at high temperatures for some materials, while QHA3P performs well. This study demonstrates that QHA3P is an ideal framework for the high-throughput prediction of finite-temperature material properties, combining the accuracy of QHA with the computational efficiency of SC-QHA.

[1] S. Curtarolo, W. Setyawan, G. L. W. Hart, M. Jahnátek, R. V. Chepulskii, R. H. Taylor, S. Wang, J. Xue, K. Yang, O. Levy, M. J. Mehl, H. T. Stokes, D. O. Demchenko, and D. Morgan, AFLOW: An automatic framework for high-throughput materials discovery, Comput. Mater. Sci. **58**, 218 (2012).

[2] S. Curtarolo, W. Setyawan, S. Wang, J. Xue, K. Yang, R. H. Taylor, L. J. Nelson, G. L. W. Hart, S. Sanvito, M. Buongiorno Nardelli, N. Mingo, and O. Levy, AFLOWLIB. ORG: A distributed materials properties repository from high-throughput *ab initio* calculations, Comput. Mater. Sci. **58**, 227 (2012).

[3] R. H. Taylor, F. Rose, C. Toher, O. Levy, K. Yang, M. Buongiorno Nardelli, and S. Curtarolo, A RESTful API for exchanging materials data in the AFLOWLIB.org consortium, Comput. Mater. Sci. **93**, 178 (2014).

[4] A. R. Supka, T. E. Lyons, L. S. I. Liyanage, P. D'Amico, R. Al Rahal Al Orabi, S. Mahatara, P. Gopal, C. Toher, D. Ceresoli, A. Calzolari, S. Curtarolo, M. Buongiorno Nardelli, and M. Fornari, AFLOWπ: A minimalist approach to high-throughput *ab initio* calculations including the generation of tight-binding Hamiltonians, Comput. Mater. Sci. **136**, 76 (2017).

[5] F. Rose, C. Toher, E. Gossett, C. Oses, M. Buongiorno Nardelli, M. Fornari, and S. Curtarolo, AFLUX: The LUX materials search API for the AFLOW data repositories, Comput. Mater. Sci. **137**, 362 (2017).

[6] H. Yu, D. Duan, H. Liu, T. Yang, F. Tian, K. Bao, D. Li, Z. Zhao, B. Liu, and T. Cui, *Ab initio* molecular dynamic study of solid-state transitions of ammonium nitrate, Sci. Rep. **6**, 18918 (2016).

[7] G. Kresse and J. Hafner, *Ab initio* molecular dynamics for open-shell transition metals, Phys. Rev. B **48**, 13115 (1993).

[8] J. Sarnthein, K. Schwarz, and P. E. Blöchl, *Ab initio* molecular-dynamics study of diffusion and defects in solid Li$_3$N, Phys. Rev. B **53**, 9084 (1996).

[9] H. L. Zhang, Y. F. Han, W. Zhou, Y. B. Dai, J. Wang, and B. D. Sun, Atomic study on the ordered structure in Al melts induced by liquid/substrate interface with Ti solute, Appl. Phys. Lett. **106**, 041606 (2015).

[10] B. J. Jesson and P. A. Madden, Structure and dynamics at the aluminum solid-liquid interface: An *ab initio* simulation, J. Chem. Phys. **113**, 5935 (2000).

[11] I. Errea, M. Calandra, and F. Mauri, First-Principles Theory of Anharmonicity and the Inverse Isotope Effect in Superconducting Palladium-Hydride Compounds, Phys. Rev. Lett. **111**, 177002 (2013).

[12] I. Errea, M. Calandra, and F. Mauri, Anharmonic free energies and phonon dispersions from the stochastic self-consistent harmonic approximation: Application to platinum and palladium hydrides, Phys. Rev. B **89**, 064302 (2014).

[13] M. A. Blanco, E. Francisco, and V. Luaña, GIBBS: Isothermal-isobaric thermodynamics of solids from energy curves using a quasi-harmonic Debye model, Comput. Phys. Commun. **158**, 57 (2004).

[14] J.-P. Poirier, *Introduction to the Physics of the Earth's Interior*, 2nd ed. (Cambridge University Press, Cambridge, U.K., 2000).

[15] O. Isayev, C. Oses, C. Toher, E. Gossett, S. Curtarolo, and A. Tropsha, Universal fragment descriptors for predicting properties of inorganic crystals, Nat. Commun. **8**, 15679 (2017).

[16] E. Gossett, C. Toher, C. Oses, O. Isayev, F. Legrain, F. Rose, E. Zurek, J. Carrete, N. Mingo, A. Tropsha, and S. Curtarolo, AFLOW-ML: A RESTful API for machine-learning predictions of materials properties, Comput. Mater. Sci. **152**, 134 (2018).

[17] C. Toher, J. J. Plata, O. Levy, M. de Jong, M. D. Asta, M. Buongiorno Nardelli, and S. Curtarolo, High-throughput computational screening of thermal conductivity, Debye temperature, and Grüneisen parameter using a quasiharmonic Debye model, Phys. Rev. B **90**, 174107 (2014).

[18] C. Toher, C. Oses, J. J. Plata, D. Hicks, F. Rose, O. Levy, M. de Jong, M. D. Asta, M. Fornari, M. Buongiorno Nardelli, and S. Curtarolo, Combining the AFLOW GIBBS and elastic libraries to efficiently and robustly screen thermomechanical properties of solids, Phys. Rev. Mater. **1**, 015401 (2017).

[19] Z. K. Liu and Y. Wang, *Computational Thermodynamics of Materials*. 1st ed. (Cambridge University Press, Cambridge, U.K., 2016).

[20] Y. Wang, Z.-K. Liu, and L.-Q. Chen, Thermodynamic properties of Al, Ni, NiAl, and Ni$_3$Al from first-principles calculations, Acta Mater. **52**, 2665 (2004).

[21] T. Duong, S. Gibbons, R. Kinra, and R. Arróyave, *Ab-initio* approach to the electronic, structural, elastic, and finite-temperature thermodynamic properties of Ti$_2AX$ ($A = $ Al or Ga and $X = $ C or N), J. Appl. Phys. **110**, 093504 (2011).

[22] P. Nath, J. J. Plata, D. Usanmaz, R. Al Rahal Al Orabi, M. Fornari, M. Buongiorno Nardelli, C. Toher, and S. Curtarolo, High-throughput prediction of finite-temperature properties using the quasi-harmonic approximation, Comput. Mater. Sci. **125**, 82 (2016).

[23] J. M. Ziman, *Electrons and Phonons: The Theory of Transport Phenomena in Solids*, Oxford Classic Texts in the Physical Sciences (Oxford University Press, Oxford, U.K., 1960).

[24] D. C. Wallace, *Thermodynamics of Crystals* (Wiley, New York, 1972).

[25] M. T. Dove, *Introduction to Lattice Dynamics*, Cambridge Topics in Mineral Physics and Chemistry (Cambridge University Press, Cambridge, U.K., 1993).

[26] G. P. Srivastava, *The Physics of Phonons* (CRC/Taylor & Francis, Oxford, 1990).

[27] S. Baroni, S. de Gironcoli, A. Dal Corso, and P. Giannozzi, Phonons and related crystal properties from density-functional perturbation theory, Rev. Mod. Phys. **73**, 515 (2001).

[28] A. van de Walle and G. Ceder, The effect of lattice vibrations on substitutional alloy thermodynamics, Rev. Mod. Phys. **74**, 11 (2002).

[29] J. J. Plata, P. Nath, D. Usanmaz, J. Carrete, C. Toher, M. de Jong, M. D. Asta, M. Fornari, M. Buongiorno Nardelli, and S. Curtarolo, An efficient and accurate framework for calculating lattice thermal conductivity of solids: AFLOW-AAPL Automatic Anharmonic Phonon Library, NPJ Comput. Mater. **3**, 45 (2017).

[30] L.-F. Huang, X.-Z. Lu, E. Tennessen, and J. M. Rondinelli, An efficient *ab-initio* quasiharmonic approach for the thermodynamics of solids, Comput. Mater. Sci. **120**, 84 (2016).

[31] R. Arroyave, D. Shin, and Z.-K. Liu, *Ab initio* thermodynamic properties of stoichiometric phases in the Ni-Al system, Acta Mater. **53**, 1809 (2005).

[32] T. Tohei, Y. Watanabe, H.-S. Lee, and Y. Ikuhara, First principles calculation of thermal expansion coefficients of pure and Cr doped α-alumina crystals, J. Appl. Phys. **120**, 142106 (2016).

[33] P. Hermet, R. M. Ayral, E. Theron, P. G. Yot, F. Salles, M. Tillard, and P. Jund, Thermal expansion of Ni-Ti-Sn Heusler and half-Heusler materials from first-principles calculations and experiments, J. Phys. Chem. C **118**, 22405 (2014).

[34] C.-L. Fu and K.-M. Ho, First-principles calculation of the equilibrium ground-state properties of transition metals: Applications to Nb and Mo, Phys. Rev. B **28**, 5480 (1983).

[35] J. Sólyom, *Fundamentals of the Physics of Solids*, Vol. 1, 1st ed. (Springer, Berlin, 2007).

[36] I. Barin, *Thermochemical Data of Pure Substances* (VCH, Weinheim, Ger., 1993).

[37] D. F. Gibbons, Thermal Expansion of Some Crystals with the Diamond Structure, Phys. Rev. **112**, 136 (1958).

[38] W. M. Yim and R. J. Paff, Thermal expansion of AlN, sapphire, and silicon, J. Appl. Phys. **45**, 1456 (1974).

[39] Y. Okada and Y. Tokumaru, Precise determination of lattice parameter and thermal expansion coefficient of silicon between 300 and 1500 K, J. Appl. Phys. **56**, 314 (1984).

[40] M. W. Chase, Jr., *NIST-JANAF Thermochemical Tables*, Journal of Physical and Chemical Reference Data Monographs, 4th ed. (American Institute of Physics, Woodbury, NY, 1998).

[41] G. A. Slack and S. F. Bartram, Thermal expansion of some diamond-like crystals, J. Appl. Phys. **46**, 89 (1975).

[42] B. J. Skinner, The thermal expansions of thoria, periclase, and diamond, Am. Mineral. **42**, 39 (1957).

[43] A. C. Victor, Heat capacity of diamond at high temperatures, J. Chem. Phys. **36**, 1903 (1962).

[44] H. J. McSkimin and P. Andreatch, Jr., Elastic moduli of diamond as a function of pressure and temperature, J. Appl. Phys. **43**, 2944 (1972).

[45] Z. Li and R. C. Bradt, Thermal expansion of the hexagonal (4*H*) polytype of SiC, J. Appl. Phys. **60**, 612 (1986).

[46] G. I. Csonka, J. P. Perdew, A. Ruzsinszky, P. H. T. Philipsen, S. Lebègue, J. Paier, O. A. Vydrov, and J. G. Ángyán, Assessing the performance of recent density functionals for bulk solids, Phys. Rev. B **79**, 155107 (2009).

[47] A. A. Khan, X-ray determination of thermal expansion of zinc oxide, Acta Crystallogr., Sect. A **24**, 403 (1968).

[48] Y. S. Touloukian, R. K. Kirby, R. E. Taylor, and P. D. Desai, *Thermophysical Properties of Matter; Thermal Expansion; Nonmetallic Solids*, Vol. 13 (IFI-Plenum, New York, 1977).

[49] H. Ibach, Thermal expansion of silicon and zinc oxide (II), Phys. Status Solidi **33**, 257 (1969).

[50] S. Kondo, K. Tateishi, and N. Ishizawa, Structural evolution of corundum at high temperatures, Jpn. J. Appl. Phys. **47**, 616 (2008).

[51] R. G. Munro, Evaluated material properties for a sintered α-alumina, J. Am. Ceram. Soc. **80**, 1919 (1997).

[52] J. B. Wachtman, Jr., T. G. Scuderi, and G. W. Cleek, Linear thermal expansion of aluminum oxide and thorium oxide from 100° to 1100° K, J. Am. Ceram. Soc. **45**, 319 (1962).

[53] *II-VI and I-VII Compounds: Semimagnetic Compounds*, edited by O. Madelung, U. Rössler, and M. Schulz (Springer, Berlin, 1999).

[54] O. L. Anderson, D. Isaak, and H. Oda, High-temperature elastic constant data on minerals relevant to geophysics, Rev. Geophys. **30**, 57 (1992).

[55] G. K. White and O. L. Anderson, Grüneisen parameter of magnesium oxide, J. Appl. Phys. **37**, 430 (1966).

[56] G. Kresse and J. Hafner, *Ab initio* molecular dynamics for liquid metals, Phys. Rev. B **47**, 558 (1993).

[57] C. E. Calderon, J. J. Plata, C. Toher, C. Oses, O. Levy, M. Fornari, A. Natan, M. J. Mehl, G. L. W. Hart, M. Buongiorno Nardelli, and S. Curtarolo, The AFLOW standard for high-throughput materials science calculations, Comput. Mater. Sci. **108**, 233 (2015).

[58] P. E. Blöchl, Projector augmented-wave method, Phys. Rev. B **50**, 17953 (1994).

[59] J. P. Perdew, K. Burke, and M. Ernzerhof, Generalized Gradient Approximation Made Simple, Phys. Rev. Lett. **77**, 3865 (1996).

[60] J. P. Perdew, A. Ruzsinszky, G. I. Csonka, O. A. Vydrov, G. E. Scuseria, L. A. Constantin, X. Zhou, and K. Burke, Restoring the Density-Gradient Expansion for Exchange in Solids and Surfaces, Phys. Rev. Lett. **100**, 136406 (2008).

[61] P. Nath, J. J. Plata, D. Usanmaz, C. Toher, M. Fornari, M. Buongiorno Nardelli, and S. Curtarolo, High throughput combinatorial method for fast and robust prediction of lattice thermal conductivity, Scr. Mater. **129**, 88 (2017).

[62] D. Hicks, C. Oses, E. Gossett, G. Gomez, R. H. Taylor, C. Toher, M. J. Mehl, O. Levy, and S. Curtarolo, AFLOW-SYM: Platform for the complete, automatic and self-consistent symmetry analysis of crystals, Acta Crystallogr., Sect. A **74**, 184 (2018).

[63] Y. Wang, J. J. Wang, W. Y. Wang, Z. G. Mei, S. L. Shang, L. Q. Chen, and Z. K. Liu, A mixed-space approach to first-principles calculations of phonon frequencies for polar materials, J. Phys.: Condens. Matter **22**, 202201 (2010).

[64] M. K. Drulis, H. Drulis, A. E. Hackemer, A. Ganguly, T. El-Raghy, and M. W. Barsoum, On the low temperature heat capacities of Ti$_2$AlN and Ti$_2$Al(N$_{0.5}$C$_{0.5}$), J. Alloys Compd. **433**, 59 (2007).

[65] D.-y. Jung, K. Kurosaki, C.-e. Kim, H. Muta, and S. Yamanaka, Thermal expansion and melting temperature of the half-Heusler compounds: *M*NiSn (*M* = Ti, Zr, Hf), J. Alloys Compd. **489**, 328 (2010).

[66] N. J. Lane, S. C. Vogel, and M. W. Barsoum, Temperature-dependent crystal structures of Ti$_2$AlN and Cr$_2$GeC as

determined from high temperature neutron diffraction, J. Am. Ceram. Soc. **94**, 3473 (2011).

[67] F. G. Aliev, V. V. Kozyrkov, V. V. Moshchalkov, R. V. Scolozdra, and K. Durczewski, Narrow band in the intermetallic compounds MNiSn ($M =$ Ti, Zr, Hf), Z. Phys. B: Condens. Matter **80**, 353 (1990).

[68] A. Togo, L. Chaput, and I. Tanaka, Distributions of phonon lifetimes in Brillouin zones, Phys. Rev. B **91**, 094306 (2015).

[69] M. J. Mehl, D. Hicks, C. Toher, O. Levy, R. M. Hanson, G. L. W. Hart, and S. Curtarolo, The AFLOW Library of Crystallographic Prototypes: Part 1, Comput. Mater. Sci. **136**, S1 (2017).

[70] D. Hicks, M. J. Mehl, E. Gossett, C. Toher, O. Levy, R. M. Hanson, G. L. W. Hart, and S. Curtarolo, The AFLOW Library of Crystallographic Prototypes: Part 2, Comput. Mater. Sci. **161**, S1 (2019).

[71] The AFLOW Library of Crystallographic Prototypes, Diamond (A4) Structure, http://aflow.org/CrystalDatabase/A_cF8_227_a.html (accessed April 30, 2019).

[72] The AFLOW Library of Crystallographic Prototypes, Wurtzite (ZnS, B4) Structure, http://aflow.org/CrystalDatabase/AB_hP4_186_b_b.html (accessed April 30, 2019).

[73] The AFLOW Library of Crystallographic Prototypes, Corundum (Al_2O_3, $D5_1$) Structure, http://aflow.org/CrystalDatabase/A2B3_hR10_167_c_e.html (accessed April 30, 2019).

[74] The AFLOW Library of Crystallographic Prototypes, Rock Salt (NaCl, B1) Structure, http://aflow.org/CrystalDatabase/AB_cF8_225_a_b.html (accessed April 30, 2019).

[75] The AFLOW Library of Crystallographic Prototypes, CsCl (B2) Structure, http://aflow.org/CrystalDatabase/AB_cP2_221_b_a.html (accessed April 30, 2019).

[76] The AFLOW Library of Crystallographic Prototypes, Half-Heusler ($C1_b$) Structure, http://aflow.org/CrystalDatabase/ABC_cF12_216_b_c_a.html (accessed April 30, 2019).

[77] The AFLOW Library of Crystallographic Prototypes, $AlCCr_2$ Structure, http://aflow.org/CrystalDatabase/ABC2_hP8_194_d_a_f.html (accessed April 30, 2019).